AIAA JOURNAL
Vol. 31, No. 10, October 1993

Multigrid Navier-Stokes Calculations for Three-Dimensional Cascades

Feng Liu*
University of California, Irvine, Irvine, California 92717
and
Antony Jameson†
Princeton University, Princeton, New Jersey 08544

A vertex-based finite volume method for solving the three-dimensional compressible Reynolds-averaged Navier-Stokes equations is presented for calculating turbomachinery cascade flows. A discretization scheme for the viscous terms is proposed. The Baldwin-Lomax algebraic turbulence model is used. The scheme is verified against laminar and turbulent flows over a flat plate. Two- and three-dimensional computations were carried out for a low-pressure turbine cascade at design and off-design conditions. Results are compared with inviscid solutions and experimental data.

I. Introduction

In an earlier paper[1] the authors presented results of cascade flow calculations with a three-dimensional Euler method. It was found that the pressure distribution on the cascade blade surface agreed well with the experimental data obtained by Hodson and Dominy[2-4] for a low-pressure turbine cascade at its design condition. When proper inlet boundary conditions were given, the Euler equations were also found to be capable of capturing the major features of secondary flow vortices caused by the convection of the inlet endwall boundary layers. However, small discrepancies existed where small separation bubbles were found in the experiment at the design condition. At an off-design condition there were large differences between the predicted pressure distributions and the experimental data due to the existence of large separation in the flowfield. For such flows it is essential to include viscous effects in the simulation. Hah[5] developed an implicit relaxation method for the Navier-Stokes equations. Chima[6] used an explicit multigrid algorithm for quasi-three-dimensional flows. Some other contributions include Davis et al.,[7] Choi and Knight,[8] and Dawes.[9]

In this paper a finite volume scheme for solving the Reynolds-averaged Navier-Stokes equations in three dimensions is presented. A vertex scheme is used in this work instead of the cell-centered scheme used in Ref. 1 for the Euler equations. It is believed that a cell-vertex scheme may have better accuracy than a cell-centered scheme on irregular meshes. In this paper an alternative discretization is used for the viscous terms, as modified from one of the schemes used by Martinelli[10] in his two-dimensional Navier-Stokes code. This new discretization avoids a potential difficulty in calculating the viscous terms when the computational mesh has kinks. A multigrid method is used to accelerate convergence. The numerical method with the Baldwin-Lomax algebraic turbulence model is used to calculate the flow in the same low-pressure turbine cascade[2-4] for which solutions of the Euler equations were obtained by the authors in Ref. 1. The usefulness and limitations of the Navier-Stokes calculations will be demonstrated through comparison of the results with those of the Euler calculations and the experiment.

Presented as Paper 92-0190 at the AIAA 30th Aerospace Sciences Meeting, Reno, NV, Jan. 6–9, 1992; received Jan. 21, 1992; revision received July 20, 1992; accepted for publication Aug. 31, 1992.

*Assistant Professor, Department of Mechanical and Aerospace Engineering. Member AIAA.

†Professor, Department of Mechanical and Aerospace Engineering. Fellow AIAA.

II. Numerical Method

After proper nondimensionalization, the Reynolds-averaged Navier-Stokes equations can be written in an integral form as

$$\frac{\mathrm{d}}{\mathrm{d}t}\int_{\Omega} W\,\mathrm{d}t + \oint_{\partial\Omega} \boldsymbol{f}\cdot\boldsymbol{n}\;\mathrm{d}S = \frac{1}{Re}\oint_{\partial\Omega} \boldsymbol{F}\cdot\boldsymbol{n}\;\mathrm{d}S \tag{1}$$

for a fixed region Ω, where W is one of five conserved scalar components: density ρ; three components of momentum ρu, ρv, and ρw; and energy ρE. The convective and viscous flux vectors are $\boldsymbol{f}$ and $\boldsymbol{F}$. Re is the Reynolds number based on the reference values in the non-dimensionalization.

The flow variables in these equations are time-averaged mean variables, and the system is closed by using the Baldwin-Lomax algebraic turbulence model.[11] We describe a vertex-based finite volume method for solving these equations. Details can be found in Ref. 12. The computational domain is divided into hexahedral cells. In a vertex scheme the flow variables are defined at the cell vertices of the hexahedral cells. A system of ordinary differential equations can be obtained by applying Eq. (1) to a supercell formed by the union of eight cells surrounding a vertex point (i, j, k) in three dimensions. Thus,

$$\frac{\mathrm{d}}{\mathrm{d}t}(\Omega_{ijk} W_{ijk}) + Q_{c,ijk} - Q_{v,ijk} = 0 \tag{2}$$

where Ω_{ijk} is the volume of the supercell and $Q_{c,ijk}, Q_{v,ijk}$ are the net convective and diffusive fluxes out of the supercell, respectively. The convective flux balance over the mth elementary cell around the vertex (i, j, k) can be approximated by

$$(Q_{c,ijk})_m = \sum_{k=1}^{6} \boldsymbol{f}_k \cdot \mathrm{d}\boldsymbol{S}_k \quad \text{for} \quad m = 1, 2, \ldots, 8 \tag{3}$$

where the summation is over the six faces of the hexahedral cell, the face area vector is $\mathrm{d}\boldsymbol{S}_k = \boldsymbol{n}\cdot\mathrm{d}S_k$, which has the face area as its magnitude and the outer normal $\boldsymbol{n}$ for its direction, and $\boldsymbol{f}_k$ are the average flux vectors on each face. The convective flux balance over one supercell can be obtained by summing the flux balances over the eight constituent cells.

$$Q_{c,ijk} \sum_{m=1}^{8} (Q_{c,ijk})_m \tag{4}$$

Since flow variables are defined at cell vertices, the velocity and temperature derivatives at each cell center can be found by applying Gauss's formula to each individual cell. Suppose $\partial u/\partial x$ is to be found at the center of a cell. By Gauss's formula,

$$\int_\Omega \frac{\partial u}{\partial x} = \int_{\partial\Omega} u \, dS_x$$

thus,

$$\Omega \frac{\partial u}{\partial x} \approx \int_{\partial\Omega} u \, dS_x$$

where dS_x is the x component of $d\boldsymbol{S}$.

To calculate the viscous flux balance $Q_{v,ijk}$ an auxiliary control volume around the vertex point (i,j,k) is formed. For simplicity, consider in Fig.1 a vertex point in a two-dimensional mesh. Martinelli[10] in one of his two-dimensional schemes formed the auxiliary control volume by directly connecting the cell centers A, B, C, and D. Since the derivatives of velocity and temperature are found at all cell centers, $\boldsymbol{F}_k$ on each face of the formed control volume can be evaluated as the average of $\boldsymbol{F}$ at the end points. $Q_{v,ijk}$ can then be obtained by

$$Q_{v,ijk} = \sum_{k=1}^{6} \boldsymbol{F}_k \cdot d\boldsymbol{S}_k \tag{5}$$

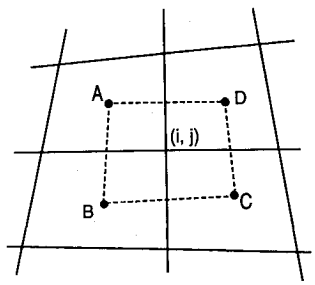

Fig. 1 Supercell and auxiliary cell for the vertex scheme.

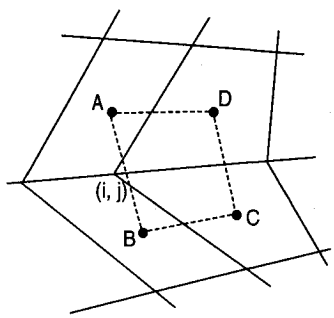

Fig. 2 Problem with a kinked mesh.

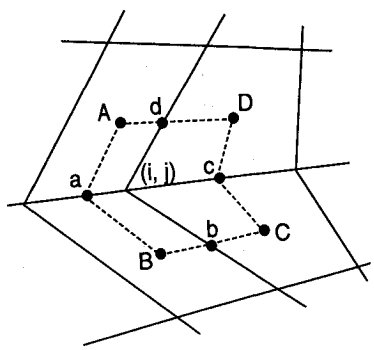

Fig. 3 Auxiliary cell used in this work to calculate the diffusive balance for the cell-vertex scheme.

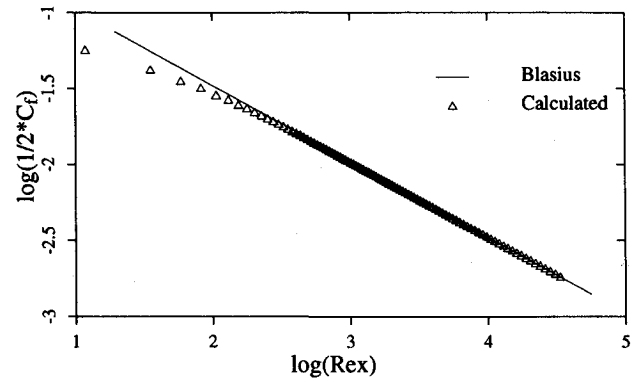

Fig. 4 Laminar skin friction coefficient over a flat plate.

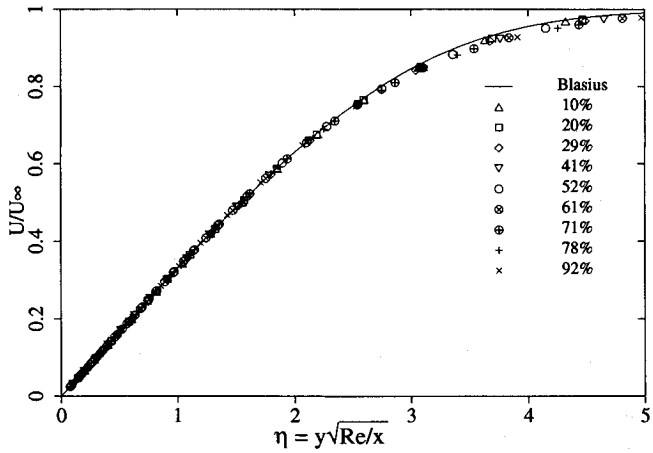

Fig. 5 Laminar boundary-layer velocity profile over a flat plate.

A difficulty may arise in this method, however, when the mesh exhibits a kink, as shown in Fig. 2. In that case, the vertex point where the diffusive flux balance is to be found falls outside the auxiliary cell, and the local accuracy may drop. To rectify this, an alternative scheme is proposed. An auxiliary cell connecting A, B, C, and D and the midpoints (midlines in three dimensions) a, b, c, and d of the cell faces is formed, as shown in Fig. 3.

The surface integral on face Aa can be evaluated as $\boldsymbol{F}_A$ times $(d\boldsymbol{S})_{Aa}$, where $\boldsymbol{F}_A$ is $\boldsymbol{F}$ at A and $(d\boldsymbol{S})_{Aa}$ is surface area vector for Aa. The surface integrals over other face segments of the control volume in Fig. 3 can be formed in the same manner. Although the surface integral on each face segment is one sided, this scheme is equivalent to Martinelli's scheme for regular meshes but is expected to give better local accuracy on grids with sharp kinks.

To prevent odd-and-even decoupling and to capture shocks without preshock oscillations, an additional dissipation term $\mathbf{D}_{ijk}$ is added to the semidiscrete Eq. (2), so that we solve

$$d/dt\,(\Omega_{ijk} W_{ijk}) + Q_{c,ijk} - Q_{v,ijk} - D_{ijk} = 0 \tag{6}$$

The dissipation term $\boldsymbol{D}_{ijk}$ is formed in a conservative manner in which the dissipation fluxes are defined as a blending of first and third differences of the flow variables. In the current applications, redistributed directionally variable dissipation scales are used (see Refs. 10 and 12).

Equation (6) can be integrated in time by an explicit multistage scheme. In this work a five-stage scheme is used, with evaluations of the dissipation and the viscous terms only at the first, third, and fifth stages. The allowable Courant-Fredrich-Lewy (CFL) number for this explicit scheme is increased by smoothing the residuals $\mathbf{R}_{ijk}$ at each stage.

$$(1-\varepsilon_\xi\delta_\xi^2)\,(1-\varepsilon_\eta\delta_\eta^2)\,(1-\varepsilon_\zeta\delta_\zeta^2)\,\bar{\boldsymbol{R}}_{ijk} = \boldsymbol{R}_{ijk} \tag{7}$$

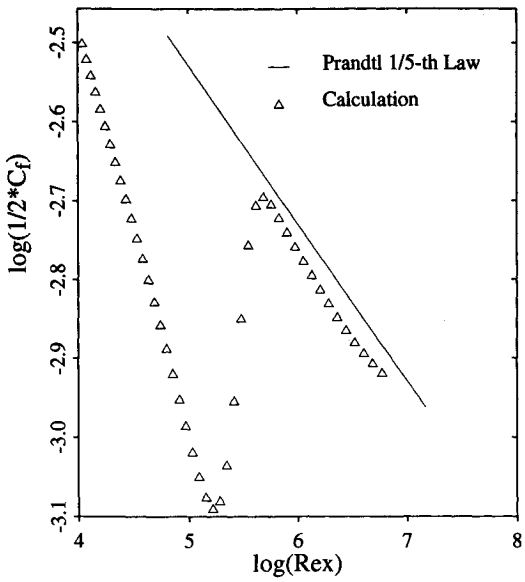

Fig. 6 Turbulent skin friction over a flat plate.

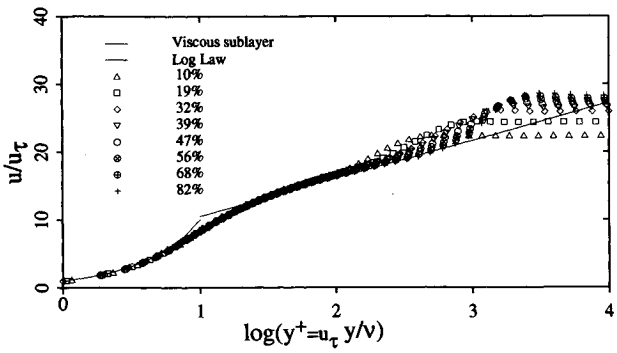

Fig. 7 Turbulent boundary-layer velocity profile over a flat plate.

where ε_ξ, ε_η, and ε_ζ are the smoothing parameters in each direction and are given by, for example,

$$\varepsilon_\xi = \max\left\{0, \frac{1}{4}\left(\frac{\mathrm{CFL}}{\mathrm{CFL}^*}\frac{\lambda_\xi}{\lambda_\xi+\lambda_\eta+\lambda_\zeta}\right)^2 - 1\right\} \tag{8}$$

CFL is the CFL number used, CFL* is the allowable CFL number for the multistage scheme, λ_ε, λ_η, and λ_ζ are the spectral radii of the Jacobian matrices of $f \cdot S_\xi$, $f \cdot S_\eta$, and $f \cdot S_\zeta$, respectively, and where S_ξ, S_η, and S_ζ are the cell surface area vectors along each grid line direction.

To further increase the rate of convergence, locally varying time steps are used. A multigrid method based on Ref. 13 is implemented. In this work a W-cycle strategy is used in each time step. In order to save computational time, the molecular and turbulent viscosity coefficients are evaluated only on the fine grid and frozen on the coarse grids. In the solution of the Reynolds-averaged Navier-Stokes equations, the robustness of the multigrid method is enhanced by smoothing the corrections from the coarse grids before they are added to the solution on the fine grids. The same factorized smoothing operator as shown in Eq. (7) is again used with a constant smoothing parameter.

III. Results and Discussion

A. Laminar and Turbulent Flow over a Flat Plate

In these calculations, the freestream Mach number is set to 0.3 to approximate incompressible flow. Laminar flow at Reynolds number Re = 35,000 is obtained. Figure 4 shows the calculated surface skin friction and that by Blasius in logarithmic scales.

A good check is the similarity profile offered by the Blasius solution. Figure 5 shows the calculated velocity profile as scaled by the Blasius similarity law at about 10, 20,..., and 90% chord length downstream of the leading edge. All of the data points collapse into a single curve on the Blasius velocity profile. Similarity is also obtained with the vertical velocities.

Turbulent flow over the same flat plate at $Re = 6 \times 10^6$ is calculated. Figure 6 is the calculated surface skin friction plotted in logarithmic scale and compared with the 1/5 law of Prandtl. In this case transition is set at $Re_x = 3.25 \times 10^5$. The skin friction jumps up at transition and then follows the 1/5 law closely toward the end of the plate.

Figure 7 shows the turbulent similarity velocity profile at different streamwise locations. Regions of laminar sublayer, the logarithmic law of the wall, and the wake are distinctly captured.

B. Flow Through a Turbine Cascade

Figure 8 is the two-dimensional mesh with 209 × 65 grid points used in the calculations. The mesh is initially generated by an elliptic method and then stretched in the blade-to-blade direction. The first grid point is taken to be 1.5×10^{-4} axial chord length away from the blade surface. In the three-dimensional calculations, only half of the blade span is used since the blade passage has a symmetric divergence of 6 deg on the sidewalls. A 209 × 65 × 33 mesh

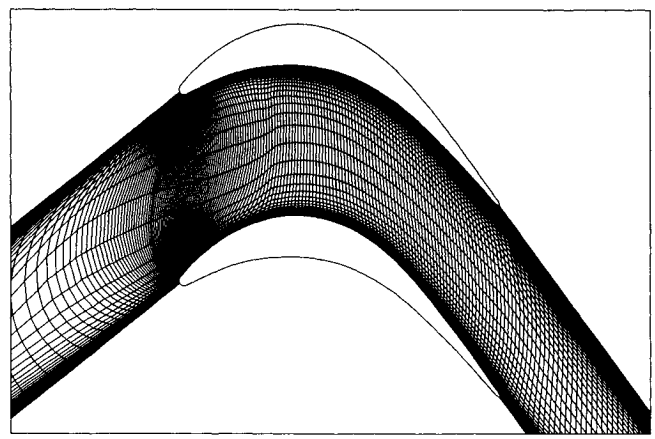

Fig. 8 H-mesh of 208 × 64 cells for a low-pressure turbine cascade.

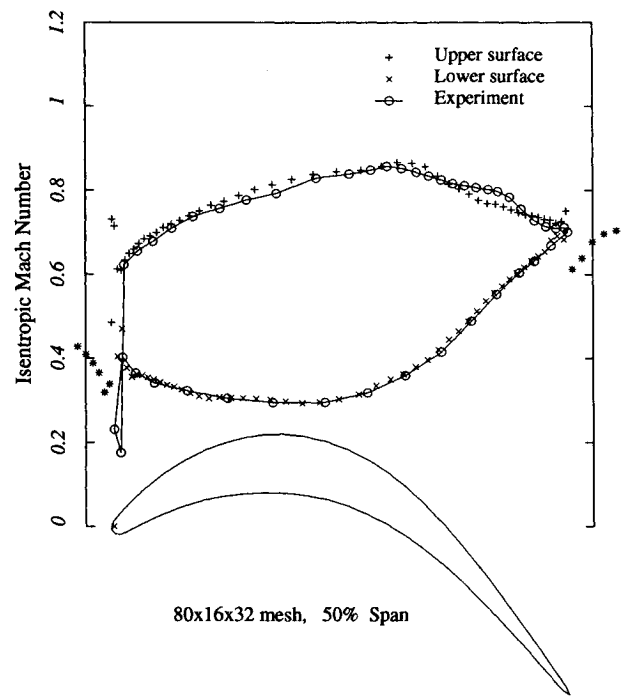

Fig. 9 Isentropic Mach number at midspan, three-dimensional Euler solution.

is generated by stacking the two-dimensional mesh in the spanwise direction. Because of the large aspect ratio of this cascade, the smallest grid size near the endwall is only 2.8×10^{-3} axial chord length.

Transitions are set at specific locations on the blade surfaces in view of experimental observations. Some adjustments of these locations were performed so that the pressure distribution agreed better with the experimental data. Such manual adjustment on transition and the turbulence model itself present major uncertainties in the calculation. On the sidewalls, experimental data in Hodson and Dominy[3] suggest that the flow is turbulent at the entrance and transitional at the exit. In the calculations, the flow is assumed to be fully turbulent on all of the endwalls. The endwall velocity profile at the entrance is specified by experimental data provided in Ref. 3.

1. Flow at the Design Condition

At its design condition this cascade has an exit isentropic Mach number of 0.7, an incidence angle of 38.8 deg, and an isentropic exit Reynolds number $Re = 2.9 \times 10^5$. Transition in this calculation is set at 0.88 axial chord on the suction surface and 0.2 axial chord

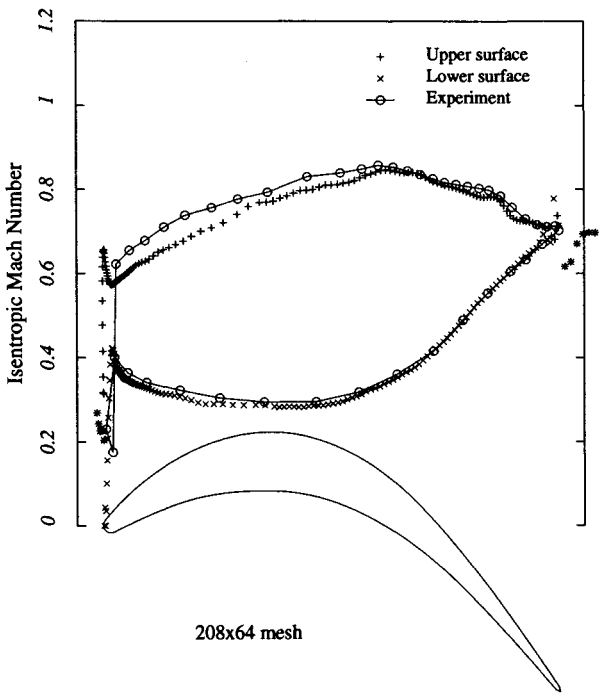

Fig. 10 Isentropic Mach number at midspan, two-dimensional Navier-Stokes solution.

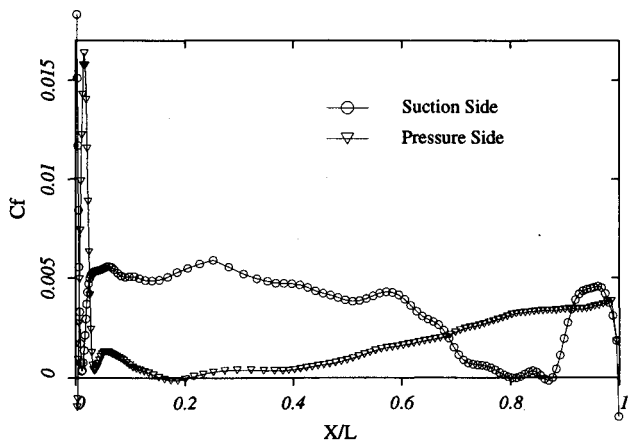

Fig. 11 Skin-friction distribution at midspan, two-dimensional Navier-Stokes solution.

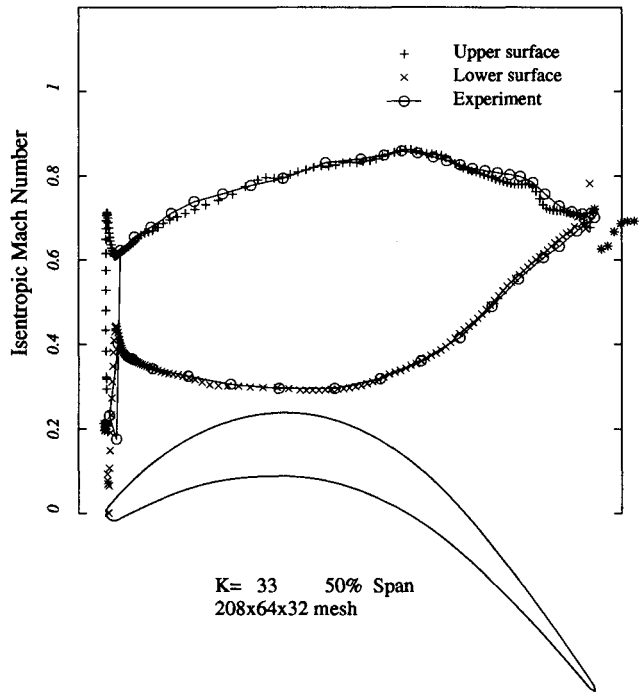

Fig. 12 Isentropic Mach number at midspan, three-dimensional Navier-Stokes solution.

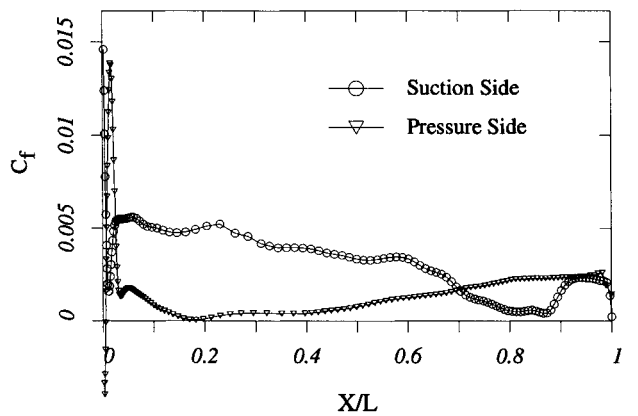

Fig. 13 Skin-friction distribution at midspan, three-dimensional Navier-Stokes solution.

on the pressure surface. Figure 9 reproduces from Ref. 1 the isentropic Mach number distribution at midspan obtained with a three-dimensional Euler method. It was explained in Ref. 1 that the slight discrepancy between calculation and experiment on the aft portion of the upper surface was due to a small separation bubble, which was observed in Hodson and Dominy's experiment.[3]

Figure 10 is the isentropic Mach number distribution at midspan calculated by the two-dimensional code. Compared with Fig. 9, the two-dimensional result underpredicts the isentropic Mach number by quite a margin due to the fact that it does not account for the divergence of the endwalls. However, the small hump in the aft portion of the suction surface pressure distribution that was observed in the experiment but missed by the inviscid calculation is now captured by the viscous code.

The separation bubble on the back of the cascade blade is confirmed by the skin friction distribution shown in Fig. 11. This separation starts at about 80% axial chord and ends at about 90% axial chord, which agrees with the experimental location obtained by oil flow in Refs. 2 and 3. It is due to this separation bubble that the isentropic Mach number in that region exhibits higher values than the inviscid solution. However, a small leading edge separation

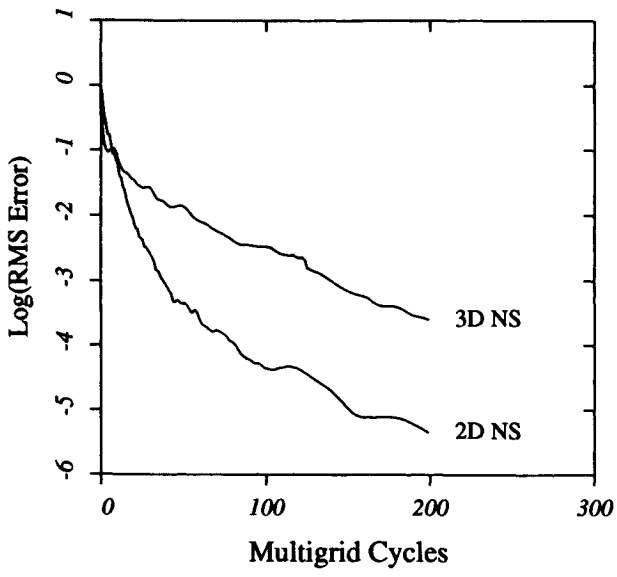

Fig. 14 Convergence history for Navier-Stokes calculations.

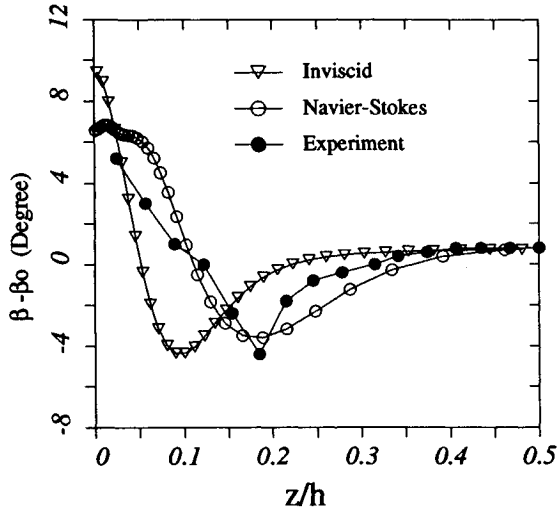

Fig. 15 Spanwise variation of pitchwise mixed-out flow angle at 140% axial chord.

bubble that was observed in experiment on the suction surface[3] is not found in this calculation, although the skin friction does show a spiked low value near the leading edge. This is most likely due to the inability of the mesh to resolve the thin boundary layer near the leading edge. On the pressure surface, incipient separation exists from about 15% axial chord to about 20% axial chord. Hodson and Dominy[2] estimated that this was from 12 to 20% blade surface distance, based on oil flow visualization.

The two-dimensional calculations capture most of the viscous features of the flow at midspan, despite the inaccuracy caused by assuming no endwall divergence. Figure 12 shows the isentropic Mach number at midspan with the three-dimensional version of the code. Clearly this problem is rectified. Figure 13 shows the skin friction distribution at midspan. Compared to the two-dimensional solution in Fig. 11, the three-dimensional solution does not predict a true separation bubble on the suction surface; rather, it predicts a small region of near separation flow. Nonetheless, the small hump in the isentropic Mach number distribution shown in Fig. 12 is closely reproduced.

The three-dimensional viscous calculation with the rather fine $209 \times 65 \times 33$ mesh takes about 12 h of CPU time in double precision on a single processor on a Convex C220 to march 200 time steps. The two-dimensional code, however, takes less than 20 min of CPU time for the same number of time steps but with better convergence. Figure 14 shows the convergence history for the two- and three-dimensional calculations. The parameters in the numerical scheme have not been optimized for the three-dimensional calculations due to constraints in computer time.

The effect of the sidewall boundary layer is closely related to secondary flow development in the cascade passage. It was shown in Ref. 1 that given the entrance sidewall boundary layer profiles, the Euler model was capable of predicting the qualitative features of the secondary flow vortices due to inviscid convection. Figure 15 contains a reproduction of the spanwise variation of pitchwise mixed-out flow angle at 140% axial chord along with those

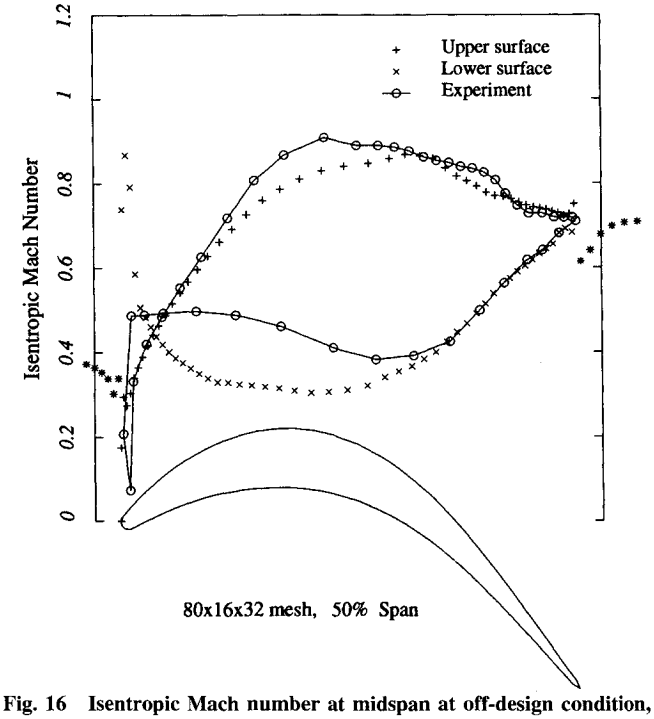

Fig. 16 Isentropic Mach number at midspan at off-design condition, three-dimensional Euler solution.

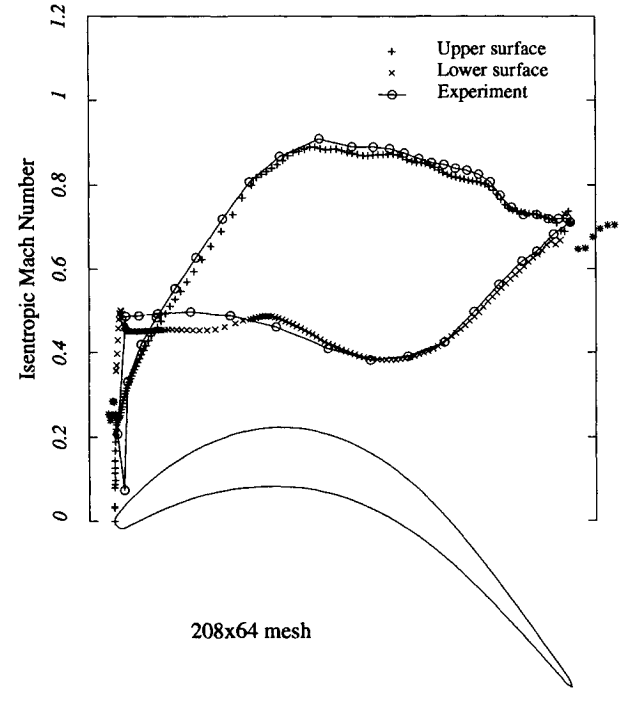

Fig. 17 Isentropic Mach number at midspan at off-design condition, two-dimensional Navier-Stokes solution.

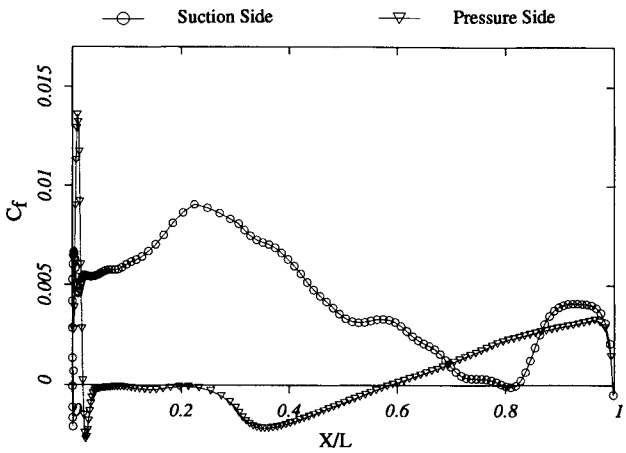

Fig. 18 Skin friction distribution at midspan at off-design condition, two-dimensional Navier-Stokes solution.

obtained by experiment[3] and the current Navier-Stokes code. The pitchwise mixed-out flow angle is obtained by a constant-area mixing calculation at each spanwise location. Essentially, the flow is extended by a fictitious constant-area pipe with uniform exit flow conditions. The uniform exit flow conditions are called the mixed-out flow conditions and can be obtained by applying the mass, momentum, and energy conservation laws. As shown in Fig. 15, there is a large overturning near the wall. This overturning is then followed by an underturning some distance into the flowfield. This is due to the induced velocity by the passage vortex. In the inviscid solution the underturning of the flow was predicted with the correct magnitude but a displaced location. The discrepancy was attributed to the fact that the Euler model does not account for the boundary layer growth in the cascade passage due to the diffusive effects of viscosity. The Navier-Stokes solution shown in Fig. 15 confirms this diffusive effect. However, the predicted magnitude of the underturning is not as large as that of the inviscid solution.

Notice also the difference between the inviscid and the viscous solutions near the endwall in Fig. 15. The overturning is reduced in the viscous solution as compared to the steady increase in the inviscid solution. The blade-to-blade pressure gradient forces the low energy flow in the boundary layer to turn more than the inviscid core flow, thus forming the passage vortex. But very near the wall, viscous effects retard this overturning mechanism. The experimental results from Hodson did not provide data very near the wall, but the existence of reduced overturning was pointed out.

2. Flow at an Off-Design Condition

Figure 16 shows the inviscid pressure distribution obtained in Ref. 1 at −20.3 deg incidence relative to the design condition. In this case there is a large separation bubble on the pressure surface. Because of this separation the inviscid solution shows a large suction peak and then a steep diffusion, as compared to the smaller suction followed by a long flat curve measured in the experiment. Figure 17 is the solution obtained with the two-dimensional Navier-Stokes code. The flat region of pressure distribution due to separation is reproduced with surprisingly good accuracy, considering the uncertainties involved in the calculation. Transition to turbulence in this calculation is set at 0.84 axial chord on the suction surface and 0 axial chord on the pressure surface. Figure 18 shows the skin friction on the blade. The pressure surface separation bubble can be clearly seen. The flow separates at about 3% axial chord and then experiences transition and reattaches at about 58% axial chord. Hodson and Dominy,[4] however, found that the separation is of a smaller length, from 5 to 45% axial chord. This may explain why the calculated isentropic Mach number tends to curve upwards compared with the experimental data. Comparison with results by other turbulence models would be desirable. Figure 19 shows the velocity vectors below the pressure surface. The large recirculation is evident.

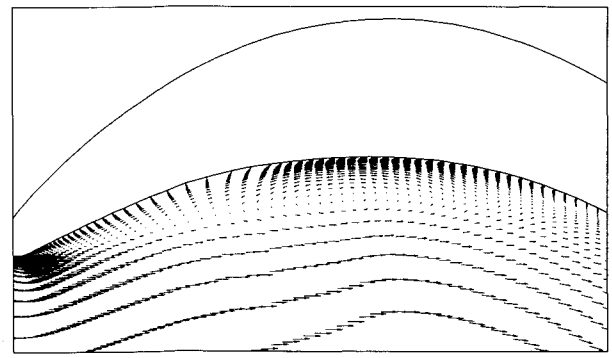

Fig. 19 Velocity vector field on the lower surface of the cascade blade.

On the suction surface, there is a small separation bubble on the back of the blade. This is confirmed by the skin friction plot and by the small hump in isentropic Mach number distribution shown in Fig. 17.

Although a steady-state solution was achieved for this case with the two-dimensional code, it was not obtained with the three-dimensional program on the $209 \times 65 \times 33$ mesh. Calculations show quite fast convergence on a coarse mesh with $105 \times 33 \times 17$ grid points. When the solution on the coarse grid is interpolated onto the fine grid, the fine grid solution converges to a certain point and then starts to oscillate, with the maximum residuals occurring in the pressure surface separation region. This may be related to the nature of the flow separation and the properties of turbulence modeling. The skin friction plot shown in Fig. 18 shows that the flow on the pressure surface has a tendency to reattach after the first separation and then separate again. In the three-dimensional calculations skin friction plots show that the flow actually reattaches with a noticeable positive skin friction and then separates. This flow behavior may have had a direct effect on the convergence of the computation. It should be pointed out, however, that Hodson and Dominy did not provide detailed skin friction measurement for this cascade, nor do the authors have knowledge of any computational results by other methods. It would be very desirable to compare results by other methods and with other turbulence models.

IV. Concluding Remarks

A vertex-based finite volume method for the Reynolds-averaged Navier-Stokes equations is presented for calculating three-dimensional cascade flows. The program has been validated by calculating laminar and turbulent flows over a flat plate. The method has been applied to a three-dimensional low-pressure turbine cascade. Clear improvements were achieved over the Euler solutions for flows with separation at both design and off-design conditions. Skin friction plots show the separation bubbles that were observed in experiment. Predicted variation of pitchwise mixed-out exit flow angle compare reasonably well with experimental data in both strength and location. However, the locations of transition and turbulence modeling pose uncertainties to the calculations. More detailed studies on the interaction between the blade and the endwall boundary layers and the development of secondary flows are needed.

Acknowledgments

This research was supported by the Office of Naval Research under Grant N00014-89-J-1366, the Defense Advanced Research Projects Agency under Grant N00014-86-K-0759, and the IBM Corporation under a Grant dated June 15, 1989. The authors are grateful for their support. The first author would also like to thank the Academic Senate Research Committee and the Office of Academic Computing at UC, Irvine for their support.

References

[1]Liu, F., and Jameson, A., "Multigrid Euler Calculations for Three-Dimensional Cascades," AIAA Paper 90-0688, Jan. 1990.

[2]Hodson, H. P., and Dominy, R. G., "Boundary Layer Transition and

Separation Observed near the Leading Edge of a High Speed Turbine Blade," *ASME Journal of Engineering for Gas Turbines & Power*, Vol. 107, Jan. 1985, pp. 127–134.

[3]Hodson, H. P., and Dominy, R. G., "Three-Dimensional Flow in a Low Pressure Turbine Cascade at its Design Condition," American Society of Mechanical Engineers Paper 86-GT-106, Dusseldorf, Germany, June 1986.

[4]Hodson, H. P., and Dominy, R. G., "The Off-Design Performance of a Low Pressure Turbine Cascade," American Society of Mechanical Engineers Paper 86-GT-188, Dusseldorf, Germany, June 1986.

[5]Hah, C., "Calculation of Three-Dimensional Viscous Flows in Turbomachinery with an Implicit Relaxation Method," *Journal of Propulsion*, Vol. 3, No. 5, 1987, pp. 415–422.

[6]Chima, R. V., "Explicit Multigrid Algorithm for Quasi-Three-Dimensional Viscous Flows in Turbomachinery," *Journal of Propulsion*, Vol. 3, No. 5, 1987, pp. 397–405.

[7]Davis, R. L., Ni, R.-H., and Carter, J. E., "Cascade Viscous Flow Analysis Using the Navier-Stokes Equations," *Journal of Propulsion*, Vol. 3, No. 5, 1987, pp. 406–414.

[8]Choi, D., and Knight, C. J., "Computation of Three-Dimensional Viscous Linear Cascade Flows," *AIAA Journal*, Vol. 26, No. 12, 1988, pp. 1477–1482.

[9]Dawes, W. N., "Development of a 3-D Navier-Stokes Solver for Application to All Types of Turbomachinery," American Society of Mechanical Engineers Paper 88-GT-70, 1988.

[10]Martinelli, L., "Calculations of Viscous Flows with a Multigrid Method," Ph.D. Dissertation, Dept. of Mechanical and Aerospace Engineering, Princeton Univ., Princeton, NJ, 1987.

[11]Baldwin, B. S., and Lomax, H., "Thin Layer Approximation and Algebraic Model for Separated Turbulent Flows," AIAA Paper 78-257, 1978.

[12]Liu, F., "Numerical Calculation of Turbomachinery Cascade Flows," Ph.D. Dissertation, Princeton Univ., Princeton, NJ, June 1991.

[13]Jameson, A., "Solution of the Euler Equations by a Multigrid Method," *Applied Mathematics and Computation*, Vol. 13, Nos. 3 and 4, 1983, pp. 327–356.